The Astronomical Journal, 118:468–476, 1999 July

THE ETCHED HOURGLASS NEBULA MyCn 18. I. *HUBBLE SPACE TELESCOPE* OBSERVATIONS

Raghvendra Sahai,[1] Aditya Dayal,[1,2] Alan M. Watson,[3] John T. Trauger,[1] Karl R. Stapelfeldt,[1] Christopher J. Burrows,[4] John S. Gallagher III,[5] Paul A. Scowen,[6] J. Jeff Hester,[6] Robin W. Evans,[1] Gilda E. Ballester,[7] John T. Clarke,[7] David Crisp,[1] Richard E. Griffiths,[8] John G. Hoessel,[5] Jon A. Holtzman,[9] John Krist,[4] and Jeremy R. Mould[10]

Received 1999 February 25; accepted 1999 March 15

ABSTRACT

We have obtained emission-line and continuum images of the young planetary nebula MyCn 18 with the Wide Field Planetary Camera 2 on the *Hubble Space Telescope* (*HST*). Although from the ground MyCn 18 appeared to have a triple-ring structure similar to SN 1987A, the *HST* images show that MyCn 18 has an overall hourglass shape. A series of arcs appear to be etched on the walls of the hourglass near its rims. In the complex central region of the nebula we find a small, inner hourglass structure and two rings. Ring 1 is a bright elliptical ring, and ring 2 a smaller, higher excitation ring. The outer and inner hourglass, and ring 1 and ring 2, all have different centers, and none are coincident with the central star. The hourglass shape of the main nebula is consistent with the predictions of the generalized interacting-winds hypothesis for planetary nebula formation. However, the complex inner nebular structure of MyCn 18 and the offset of the central star from the center of the nebula remain a mystery. We discuss several mechanisms for producing the offset of the central star. Although none are found to be completely satisfactory, those involving a binary central star probably offer the best hope of successful explanation.

Key words: circumstellar matter — ISM: kinematics and dynamics — planetary nebulae: individual (MyCn 18) — stars: AGB and post-AGB — stars: mass loss

1. INTRODUCTION

MyCn 18 (PK 307−4°1) is a planetary nebula (PN) named after its discoverers, Mayall & Cannon (1940). Schwarz, Corradi, & Melnick (1992) obtained ground-based images that show a striking resemblance to the triple-ring nebula around SN 1987A (Burrows et al. 1995). Corradi & Schwarz (1993, hereafter CS93) obtained images and long-slit spectra of MyCn 18 and concluded from optical and near-infrared diagnostics that it is a young PN. The Of(h) central star has an effective temperature of 51,000 K. The nebular expansion velocity determined from [O III] λ5007 emission is 10 km s^{-1} (Gleizes, Acker, & Stenholm 1989), lower than the value indicated by the 48 km s^{-1} velocity spread seen in the [N II] λ6548 spectrum (CS93). As is true for most PNs, the distance to MyCn 18 is uncertain, with estimates spanning a broad range from 800 to 3200 pc. More recent determinations favor larger distances, and in this paper we have followed CS93 and adopted 2.4 kpc.

We have obtained images of MyCn 18 with the Wide Field Planetary Camera 2 (WFPC2) on the *Hubble Space Telescope* (*HST*). We present these images here and use them to investigate the structure of MyCn 18. In § 2 we describe our observations. In § 3 we present our observational results. In § 4 we discuss how the nebula might have formed. In § 5 we summarize our results and conclusions. Detailed spatio-kinematic modeling of the nebula, which will be of particular use to theorists attempting to match gasdynamic models to this nebula, is presented in a following paper (Dayal et al. 1999, hereafter Paper II).

2. OBSERVATIONS

MyCn 18 was imaged using the Planetary Camera of WFPC2, which has a field of view of 34″ × 34″ and scale of 0″.0456 $pixel^{-1}$ (Trauger et al. 1994). Observations were made in four narrowband filters dominated by [O I], [N II], Hα, and [O III] emission lines and one line-free medium-band filter (F547M). Table 1 is a summary of the observations. Standard procedures were used to reduce and calibrate the images. Cosmic rays were removed by comparing two equal-exposure images, when available, or by scanning through the images with a 5 × 5 pixel window, determining all pixels with intensity 3 σ above the median value, and replacing them with nearest-neighbor interpolated values.

3. RESULTS

Figure 1 shows images of the whole nebula, and Figure 2 shows images of the central region in each of our filters. The Hα and [N II] emissions are similarly distributed and clearly show an hourglass-shaped nebula. The measured fluxes of the nebula are given in Table 1. The Hα flux has

[1] Jet Propulsion Laboratory, Mail Stop 183-900, California Institute of Technology, 4800 Oak Grove Drive, Pasadena, CA 91109.
[2] Infrared Processing and Analysis Center, Mail Stop 100-22, California Institute of Technology, Pasadena, CA 91125.
[3] Instituto de Astronomía, Universidad Nacional Autónoma de México, J. J. Tablada 1006, 58090 Morelia, Michoacán, Mexico.
[4] Space Telescope Science Institute, 3700 San Martin Drive, Baltimore, MD 21218.
[5] Department of Astronomy, University of Wisconsin at Madison, 475 North Charter Street, Madison, WI 53706.
[6] Department of Physics and Astronomy, Arizona State University, Tyler Mall, Tempe, AZ 85287.
[7] Department of Atmospheric, Oceanic, and Space Sciences, University of Michigan, 2455 Hayward Street, Ann Arbor, MI 48109.
[8] Department of Physics, Carnegie Mellon University, 5000 Forbes Avenue, Pittsburgh, PA 15213-3890.
[9] Department of Astronomy, New Mexico State University, Box 30001, Department 4500, Las Cruces, NM 88003-8001.
[10] Mount Stromlo and Siding Spring Observatories, Australian National University, Weston Creek Post Office, ACT 2611, Australia.

TABLE 1

SUMMARY OF *HST* WFPC2 OBSERVATIONS

Filter	Integration Time (s)	Line	Measured Flux
F656N	600	Hα	4.13×10^{-11} ergs s^{-1} cm^{-2}
F658N	700	[N II]	3.43×10^{-11} ergs s^{-1} cm^{-2}
F631N	700	[O I]	1.77×10^{-11} ergs s^{-1} cm^{-2}
F502N	700 × 2	[O III]	7.44×10^{-11} ergs s^{-1} cm^{-2}
F547M	200	Continuum	9.8 mJy

NOTES.—The Hα image suffers from contamination by [N II] because F656N has about 4% transmission at [N II] λ6586 and 29% transmission at [N II] λ6548. The [N II] 6548 Å line is one-third the strength of [N II] λ6586 in PNs, on both observational (Acker et al. 1989) and theoretical grounds; hence the combined effect is equivalent to a 14% contamination by λ6586 (see, e.g., Harrington et al. 1997). Because the [N II] λ6586 flux is ≈83% of the Hα flux, the corrected Hα flux should be ≈12% lower than the F656N flux value given above; correspondingly, contamination of [N II] λ6586 by Hα implies that the correct [N II] λ6586 flux is ≈5% less than the F658N flux value given above.

been corrected for contamination by [N II] λ6548 emission, using our measured [N II] λ6586 flux and the filter transmission curves. Acker et al. (1989) give Hα and [O III] fluxes of 8.3×10^{-11} and 2×10^{-11} ergs s^{-1} cm^{-2}, but these values are based on extrapolating the flux measured through a 4″ × 4″ aperture to the full size of the nebula (details about the extrapolation are not available) and are likely to be inaccurate.

Visual inspection of the Hα and [N II] images suggests that the top (southeastern) half of the hourglass is tilted toward us, an orientation consistent with published spectroscopic data (CS93).[11]

The F547M image is dominated by nebular *continuum* emission, rather then weak *line* emission or scattered light from the star. The only significant nebular line in the filter is [N II] λ5755, whose strength relative to Hα suggests that it contributes less than 3% of the observed emission (Acker et al. 1989). The theoretical ratio of nebular continuum to Hα flux suggests that the former has a flux density of about 9.5 Jy (Osterbrock 1989; Brown & Mathews 1970). The closeness of this to the 9.8 Jy we measure suggests that light scattered by dust makes an insignificant contribution. This conclusion is further bolstered by the similarity between the radial profiles in Hα and continuum emission (Fig. 3).

3.1. *Components and Structure of the Nebula*

We now describe the different structural components of MyCn 18, together with the relative distribution of Hα, [N II], and [O III] emission (Fig. 4). Figure 4*a* is a false-color image showing the [N II] (*red*), Hα (*green*), and [O III] (*blue*) emission; each image has been processed to emphasize sharp structures. The color balance has been adjusted such that regions where the [N II] and Hα overlap appear orange. In Figure 4*b*, we show the [N II]/Hα (*left*) and [O III]/Hα (*right*) ratio images. The false-color and ratio images show that (as expected) the [O III] emission, a tracer of higher excitation gas, is more centrally confined than the [N II] emission, a tracer of lower excitation gas—the [O III]/[N II] intensity ratio in the outer, orange regions is smaller by factors of about 30–100 compared with the greenish-blue central region. The line ratio images will be useful for constraining detailed photoionization models of the MyCn 18 nebula; such modeling is outside the scope of this paper.

The nebular structure can be divided into several distinct regions as a function of observed distance from the geometric center of the nebula. Outside the bright hourglass walls, there is weak emission with both smooth and filamentary components. This emission is visible only in the [N II] and Hα images. At both ends of the hourglass we find a bright rim, followed by a region of mottled emission. The mottled structure is seen prominently in the more distant part of the southeast rim and the nearer part of the northwest rim. The elongated knots in the mottled region are roughly 2–5 pixels (220–550 AU) wide and 5–10 pixels (550–1100 AU) long. It is difficult to determine whether any mottled structure is present in the other sides of the hourglass, because of foreshortening. Moving inward, we find a region characterized by a system of arcs. These resemble etchings on the walls of an hourglass. The etchings have FWHM of roughly 4–6 pixels (440–660 AU). Both the mottled structure and the etchings show a greater contrast relative to neighboring nebulosity in [N II] than in Hα (see Fig. 4*b*, *left*); the values of the [N II] contrast ratio lie in the range 1.7–2.5 and are typically 10%–35% higher than those for Hα. The mottling and etchings disappear at smaller radii, and the walls of the hourglass present a smoother appearance. The [N II]-to-Hα ratio is higher in the etched/mottled regions by a factor of 1.5 compared with the smooth region (see Fig. 3). The nebula measures about 18″ along its long axis and has a maximum width of about 8″.5.

In the innermost region, we find a pair of intersecting elliptical rings that appear to be the rims of a small inner hourglass (see Fig. 2*a*). Within this hourglass we find ring 1, a bright, roughly elliptical ring (size 1″.8 × 1″.4; Fig. 2*b*) that delineates the waist of the hourglass structures. Within ring 1 is ring 2, a smaller *incomplete* ring of size 0″.8 × 1″.2 (Fig. 2*d*). Ring 2 is seen prominently in Hα and [O III] but is almost invisible in [N II] and [O I]. This indicates that it consists of more highly excited gas than ring 1, presumably because it is closer to the central star. There is a local minimum of emission in the central region of ring 1.

[11] The sign of the declination increments in their long-slit spectrum is flipped (H. Schwarz 1995, private communication).

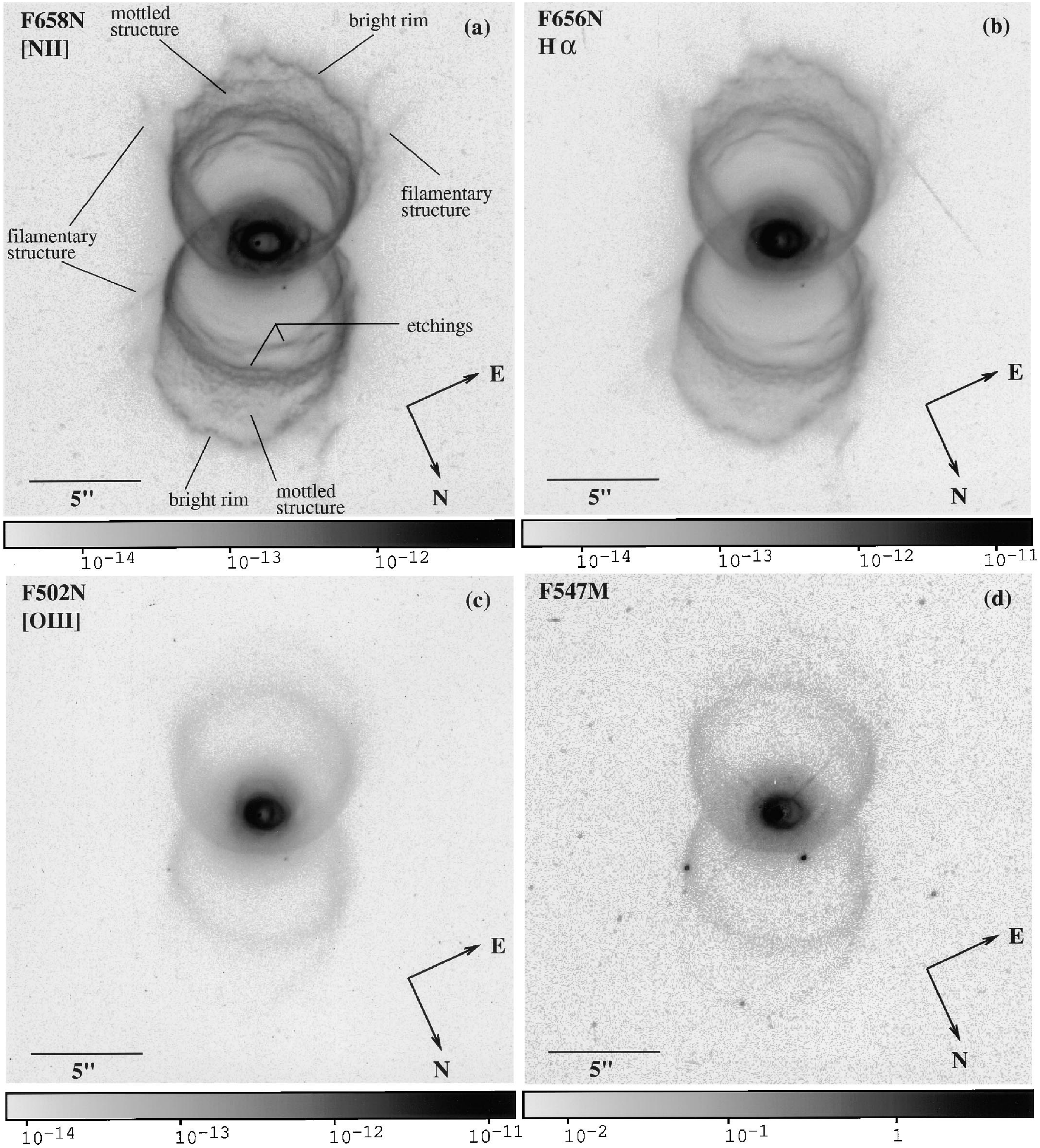

FIG. 1.—Images of the young planetary nebula MyCn 18 taken through narrowband filters with the *HST* WFPC2 to isolate atomic (or ionic) line emission. (*a*) F658N ([N II] λ6586), (*b*) F656N (Hα), (*c*) F502N ([O III] λ5007), and (*d*) a continuum filter, F547M. The plate scale is 0″.0456 pixel^{-1}, and the images cover an area 22″.8 × 22″.8 (500 × 500 pixels). The linear streak in the upper right quadrant of the Hα image is due to imperfect removal of a cosmic-ray event. A logarithmic stretch has been used in all images, and the maximum (*black*) and minimum (*white*) intensity values on the reverse gray scales (shown below each image) are (*a*) 8.43×10^{-12} and 2.93×10^{-15} ergs s^{-1} cm^{-2} arcsec^{-2}; (*b*) 1.81×10^{-11} and 3.67×10^{-15} ergs s^{-1} cm^{-2} arcsec^{-2}; (*c*) 1.47×10^{-11} and 7.38×10^{-15} ergs s^{-1} cm^{-2} arcsec^{-2}; and (*d*) 6.53 and 5.95×10^{-3} mJy arcsec^{-2}.

Moving to much larger scales, Figure 5 shows a false-color image from all four WFPC2 cameras of the region around the bright nebula. Of particular interest are the blobs of distant, faint nebulosity located along the long axis of the nebula. The blobs are fainter in [O III] than in Hα or [N II], and they appear to lie at a projected distance of 33″, or 1.3×10^{18} cm, from the center of MyCn 18. They probably belong to the larger collection of blobs representing a

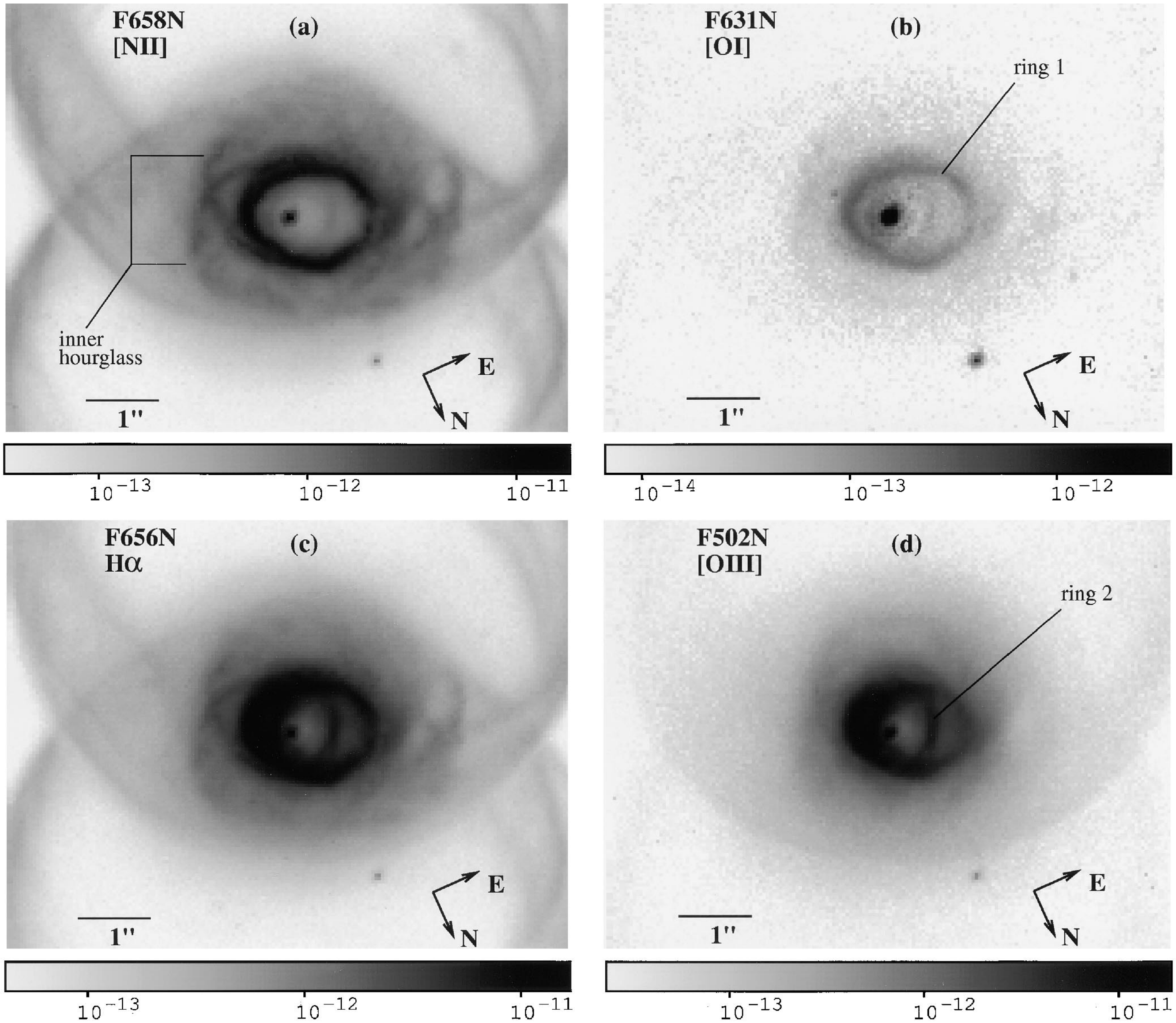

FIG. 2.—Inner 7$''$.75 × 5$''$.92 region of the nebula, seen in the emission lines of (*a*) [N II] (*b*) [O I] (*c*) Hα, and (*d*) [O III]. A logarithmic stretch and reverse gray scale have been used in all images, and the maximum (*black*) and minimum (*white*) intensity values on the reverse gray scales used (shown below each image) are (*a*) 1.79×10^{-11} and 3.56×10^{-14} ergs s^{-1} cm^{-2} arcsec^{-2}; (*b*) 3.53×10^{-12} and 6.69×10^{-15} ergs s^{-1} cm^{-2} arcsec^{-2}; (*c*) 1.67×10^{-11} and 4.19×10^{-14} ergs s^{-1} cm^{-2} arcsec^{-2}; and (*d*) 1.85×10^{-11} and 2.33×10^{-14} ergs s^{-1} cm^{-2} arcsec^{-2}.

knotty, bipolar 500 km s^{-1} outflow from MyCn 18 (Bryce et al. 1997). A rough estimate of the mass of ionized gas within each of these blobs derived from their Hα flux, assuming $T_e = (0.5\text{–}2) \times 10^4$ K, is a few times 10^{-5} $M_\odot$. The mass of these blobs can be compared with the total nebular mass of MyCn 18, estimated by modeling its *IRAS* far-infrared fluxes using the two-component dust emission model of Sahai et al. (1991) (and scaling by a typical gas-to-dust ratio). The color-corrected *IRAS* fluxes used are 2.0, 22.5, 22.4, and 12.6 Jy at 12, 25, 60, and 100 μm. Assuming a dust emissivity of 150 cm^2 g^{-1} at 60 μm (Jura 1986), with a λ^{-p} power-law variation and $p = 1.0$ (1.5), we find that the masses and temperatures of the two components are 3.3 (5.6) $\times 10^{-4}$ and 0.4 (1.1) $\times 10^{-6}$ $M_\odot$ and 89 (75) and 160 (132) K. We convert this to a total nebular mass of approximately 0.02–0.1 $M_\odot$, using the poorly known gas-to-dust ratio in PNs, which spans a range of values from 50 in the Ring Nebula (Zhang et al. 1994) to the 200 that is typical of the circumstellar envelopes (CSEs) of asymptotic giant branch (AGB) stars. The size of the thermally emitting dust region is roughly comparable to the optical nebula seen in the *HST* images: given a bolometric luminosity $L_{\rm bol}$ of 990 $L_\odot$ (§ 3.3) and $T_{\rm eff} = 51{,}000$ K, we find that dust grains reach the temperature derived above at a distance of about 5×10^{17} cm from the central star (see, e.g., Herman, Burger, & Penninx 1986; Zhang et al. 1994). We conclude that the mass of gas ejected in the high-velocity blobs is a factor 10^{-3} or less of the total nebular mass of MyCn 18.

3.2. *Centers and Misalignments*

The strong symmetry of the nebular structures in MyCn 18 allows us to locate their centers accurately and show that the outer and inner hourglasses, ring 1, and ring 2 have different centers and that none of them are centered on the central star. The major axis of the nebula has a position angle of 152° ± 0°.5. The central star does not lie on the

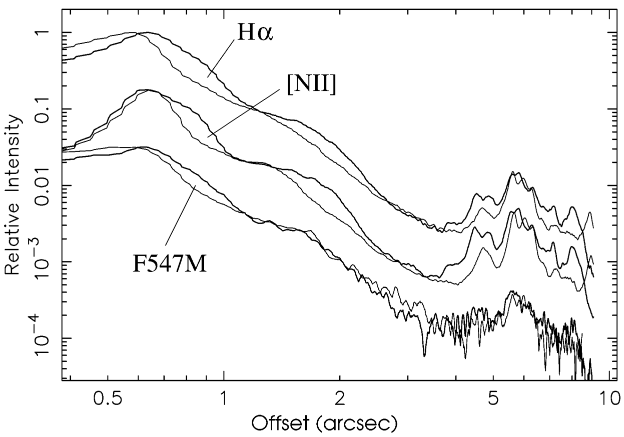

FIG. 3.—Radial cuts of the relative Hα, [N II], and continuum intensities taken along the long axis of the nebula, generated from the F656N, F658N, and F547M filter images. The intensity traces for each filter have been scaled by arbitrary factors to avoid overlap. The thin and thick curves refer to the northwest and southeast lobes of the nebula, respectively.

major axis but is offset along the minor axis (roughly westward) from the geometric centers of the outer hourglass, the inner hourglass, ring 1, and ring 2 by 2.5 ± 0.5 pixels (270 AU), 10.5 ± 1 pixels (1150 AU), 6 ± 0.5 pixels (650 AU), and 4 ± 0.5 pixels (440 AU), respectively. The greater relative brightnesses of the western sides of ring 1 and ring 2 in Hα and [O III] appear to be consistent with the central star's offset to the west.

3.3. *Central Star*

Photometry of the central star in F547M image gives $m_V = 14.90 \pm 0.05$. This implies a blue magnitude $m_B = 14.47 \pm 0.05$ (ignoring interstellar extinction) for $T_{\rm eff} = 51{,}000$ K, in agreement with the ground-based value of $m_B = 14.4 \pm 0.5$ (Tylenda et al. 1991). The bolometric flux estimated by integrating the observed flux distribution (CS93) over all wavelengths (from 0.36 to 100 μm) is 5.5×10^{-9} ergs s^{-1} cm^{-2}, yielding a luminosity $L_{\rm bol} \approx 990$ $L_\odot$ for a distance of 2.4 kpc. The above derivation is likely to underestimate $L_{\rm bol}$, because large parts of the nebula are density bounded (Paper II), allowing a significant fraction of the stellar radiation at wavelengths less than 912 Å to escape undetected from the nebula. The central star is probably surrounded by hot dust in the waist region because the expected K-band photospheric flux of 0.016 Jy is significantly smaller than the observed value of 0.033 Jy (Acker et al. 1992).

The star seen about 2″.3 north of the central star is probably a field star seen in projection against the nebula. Even if it were located within the nebula, it is too far away from the central star to have affected its evolution.

4. FORMATION OF THE ETCHED HOURGLASS NEBULA

4.1. *Large Hourglass Structure*

What physical mechanism can produce the exquisite shape and structure of the Etched Hourglass Nebula? In the generalized interacting stellar winds model (GISW) for the formation of planetary nebulae (Kwok, Purton, & Fitzgerald 1978; Balick 1987), axisymmetric PN shapes result when a fast (1000–2000 km s^{-1}), tenuous, post-AGB stellar wind expands within a slower (10–20 km s^{-1}), denser AGB CSE. The asymmetry may be intrinsic to the slow CSE (Balick 1987) or may be created by high-velocity (~ 100 km s^{-1}) collimated outflow(s) acting on an intrinsically round CSE (Sahai & Trauger 1998, hereafter ST98). Such high-velocity outflows are being discovered in an increasing number of young post-AGB objects (e.g., CRL 2688: Young et al. 1992; Sahai et al. 1998a; HD 101584: te Lintel Hekkert, Chapman, & Zijlstra 1992). In MyCn 18, the high-velocity knotty bipolar outflow (Bryce et al. 1997) favors the proposal by ST98.

Numerical models of the hydrodynamics of such interacting winds (Balick, Preston, & Icke 1987) produce a dense shell of swept-up gas with an hourglass shape when the equatorial-to-polar density contrast in the AGB CSE is relatively large ($\gtrsim 10$). The open-ended hourglass geometry and the weak, filamentary emission seen in the [N II] and Hα images outside the hourglass indicate that the fast outflow has broken out of the confining shell of swept-up gas along the polar directions into a surrounding, more tenuous CSE (Garcia-Segura & Mac Low 1994). The thin shell of compressed gas that forms the walls of the hourglass is subject to various instabilities, including the Kelvin-Helmholtz, the Rayleigh-Taylor, and the "nonlinear thin shell" (Vishniac 1994) instabilities. These instabilities will act to produce locally overdense regions (Blondin & Lundqvist 1993; Dwarkadas & Balick 1998). Indeed, the arclike etchings and mottlings appearing on the walls of the hourglass may be manifestations of such instabilities (Garcia-Segura et al. 1998). Borkowski, Blondin, & Harrington (1997) have presented two-dimensional numerical hydrodynamic modeling of a poorly collimated outflow expanding into a confining ambient medium to simulate the structure of the proto–planetary nebula He 3-1475. The results of this simulation include the formation of a thin-walled shell, which is smooth closer to the center of the nebula, but broken up further away as a result of dynamical instabilities (see Fig. 3 of Borkowski et al. 1997), qualitatively resembling the case of MyCn 18, where the etchings and mottlings appear only in the more distant regions of the hourglass walls. Alternatively, the etchings may be the remnants of thin dense shells in the progenitor AGB CSE, similar to the arcs found in the proto–planetary nebula CRL 2688 (Sahai et al. 1998b).

It is difficult to accurately constrain the properties of the progenitor dense AGB CSE that evolved into MyCn 18 without the aid of detailed hydrodynamic modeling. However, we can make rough estimates of its mass-loss timescale and mass-loss rate. From our spatio-kinematic model in Paper II, we find that (1) the mass of ionized gas in the hourglass walls is 0.013 $M_\odot$, (2) the expansion timescale for the walls is 1000–2000 yr, and (3) the density of the hourglass at a latitude of 32° (or $R = 1.3 \times 10^{17}$ cm) is about 1350 cm^{-3}. We conservatively take the density of the undisturbed AGB CSE at this radius to be a factor of 3 lower to fit the large (a factor of ~ 10) contrast in brightness between the Hα intensity in the hourglass walls and neighboring locations on the outside of the walls. Numerical GISW models of bipolar PNs with radiative losses show that this density contrast factor varies from ≈ 2 to 10 going from low to high latitudes (Mellema 1993). This would imply an AGB mass-loss rate $\dot{M}_{\rm AGB} = 2 \times 10^{-6}$ $M_\odot$ yr^{-1}, assuming a typical AGB mass ejection velocity of $V_{\rm AGB} = 10$ km s^{-1}. Although we do not directly know what fraction of the AGB CSE (within a radius of $\sim 3 \times 10^{17}$ cm) has been swept up into the hourglass shell, it clearly must be a

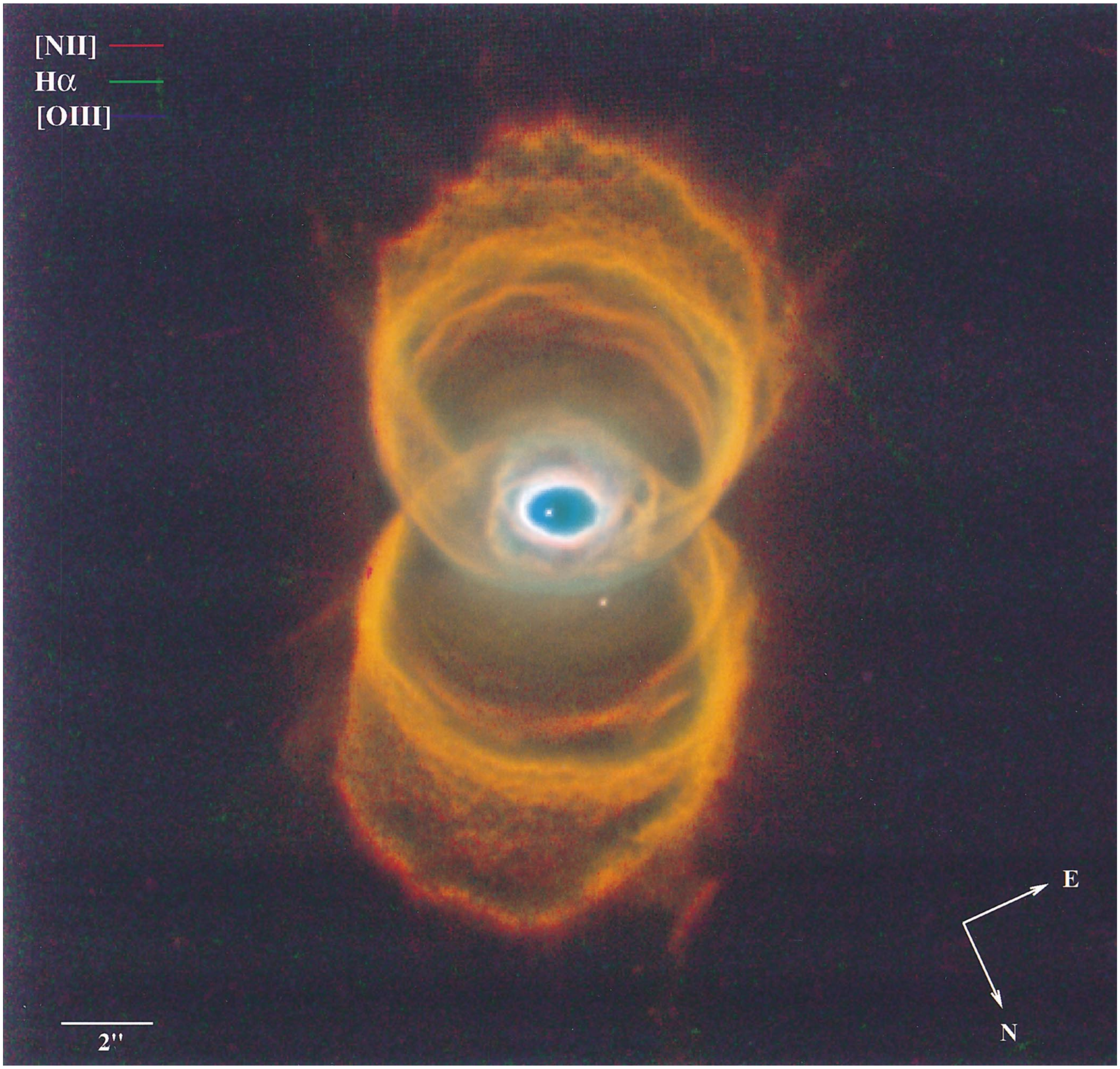

FIG. 4*a*

FIG. 4.—(*a*) Composite color image of MyCn 18 showing Hα (*green*), [N II] (*red*), and [O III] (*blue*) emission (the color balance has been adjusted such that regions where the [N II] and Hα overlap appear orange). The image covers an area 24".59 × 23".32 (540 × 512 pixels). These images have been processed to emphasize sharp structures. The processed image $\mathrm{Im}_P = \mathrm{Im}_O/(\mathrm{Im}_O + 0.04\mathrm{Im}_S)$, where Im_O is the original image and Im_S is obtained by smoothing Im_O. The greenish linear streak in the upper right quadrant of the image is due to imperfect removal of a cosmic-ray event during the Hα exposure. (*b*) *Left*: [N II]/Hα ratio image, shown on a logarithmic scale; the maximum and minimum values of the ratio on the gray scale used (shown alongside) are 0.134 and 1.48. Regions of the ratio image where the Hα image has relatively low signal-to-noise ratio have been masked and shown in green. *Right*: Same as the left panel but for [O III]/Hα; maximum and minimum ratios on the gray scale used are 0.055 and 1.76.

significant fraction because the fast outflow has already broken out of the dense CSE. Assuming this fraction to be $\frac{1}{2}$ and knowing the mass of the hourglass walls, we derive an AGB mass-loss timescale (at a radius of 3×10^{17} cm) of $\tau_{\mathrm{loss}} \approx 13{,}000$ yr, a value roughly consistent with the 11,000 yr required for the slow wind to reach the observed size of the nebula, and significantly larger than the expansion timescales for the hourglass walls.

4.2. *Central Region*

The GISW model can qualitatively explain important features of the hourglass structure in MyCn 18, but it does not address the complexities of the central region. These include the existence of the inner hourglass and ring 2, as well as the offsets of the central star from the geometric centers of the outer and inner hourglasses, ring 1, and ring 2.

The inner hourglass, like the outer hourglass, might also be produced by interacting winds. This would require the presence of a second, equatorially concentrated, dense, slowly expanding CSE interacting with a fast wind. Such a scenario has not been considered in the GISW model.

We have considered several mechanisms for producing the offset of the visible central star from the symmetry

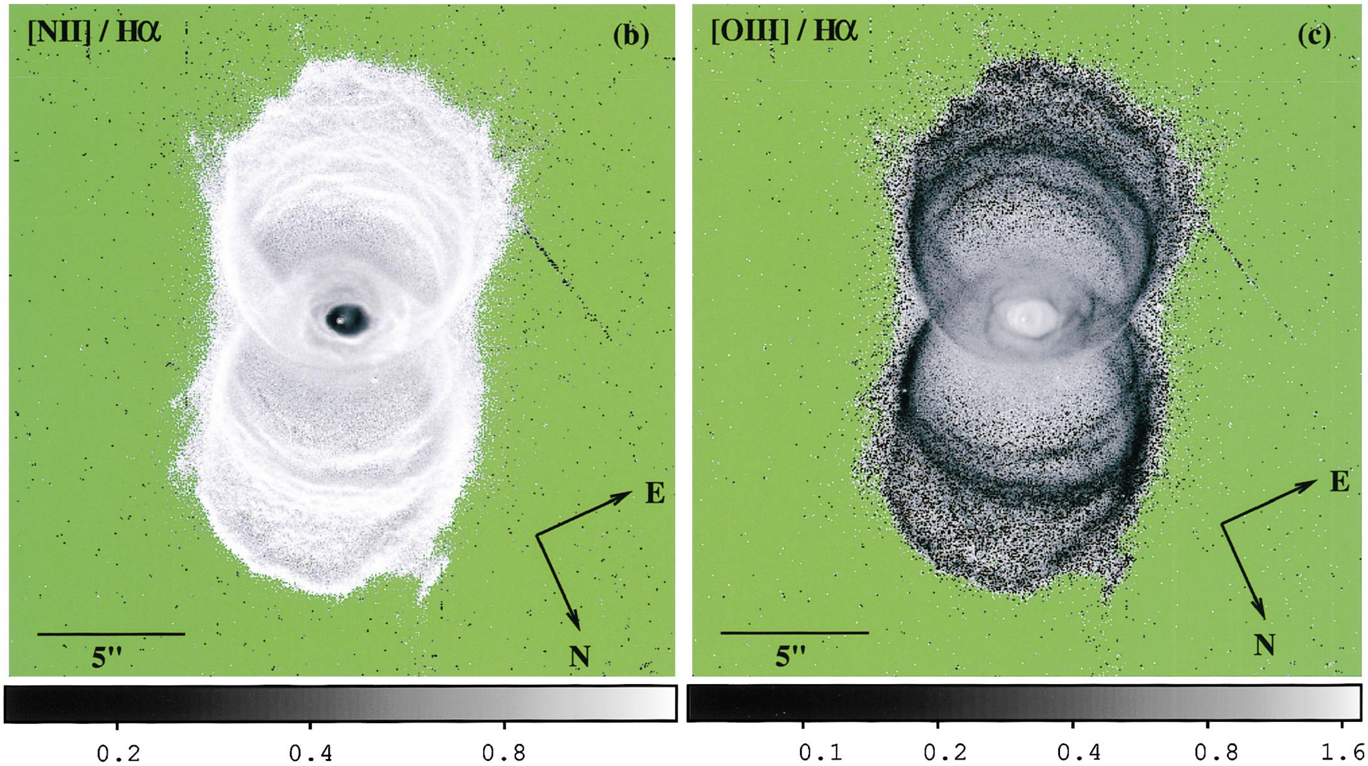

FIG. 4*b*

center of the outer hourglass. The simplest of these is that the nebula and the central star have an appreciable motion relative to the ambient ISM to the southwest, the direction of the offset. The ram pressure of the ISM on the swept-up hourglass shell would reduce its proper motion relative to the star and produce the observed offset. There are two problems with this mechanism. First, there is no obvious morphological signature on the southwest side of the nebula indicating an external pressure—the nebula is remarkably symmetric. Second, the dynamical timescale of the waist of the outer hourglass (ring 1) is $(2 \times 10^{16}$ cm)/(10 km $s^{-1}) \approx 700$ yr.[12] This timescale is small compared with the 3500 yr sound-crossing time across the approximately 10^{17} cm path through the progenitor AGB CSE, which presumably surrounds the ionization-bounded waist of the nebula. The sound-crossing time is limited by the sound speed, which is no greater than 10 km s^{-1} in ionized gas and significantly less in the lower temperature neutral gas.

We now discuss mechanisms for producing the central star offset through an asymmetric mass ejection of the progenitor AGB CSE. The first mechanism invokes a proper motion given to the star as a reaction to an intrinsic asymmetry in the mass ejection of the progenitor AGB star. Over the course of a rotation period, the net reaction force on the star will of course be zero. Thus, the reaction must have acted for a time that is less than the rotational period of the progenitor AGB star (probably less than a few hundred years, scaling from the Sun's rotation period), and the star must have traveled to its current position in this time. This requires a proper motion of order 10 km s^{-1} and a force of order 0.05 $M_{\odot}$ km s^{-1} yr^{-1}. This is significantly greater than the reaction that can be extracted from the wind ($< \dot{M}_{AGB} V_{AGB}$), which is of order 10^{-5} $M_{\odot}$ km s^{-1} yr^{-1}.

A second mechanism is one in which the central star is a close binary, with the more evolved star being the visible central star in our images. Mass transfer onto the surface of this star might have resulted in an explosive event that produced an expanding shell of ejecta and formed ring 1. The center of mass of this shell would share the same velocity as the star in its orbital motion at the time of ejection, and because it would not be gravitationally bound to the binary system, it would move away from the binary system. We reject this model for the following reasons: First, the explosive event, qualitatively similar to a nova outburst caused by thermonuclear runaway, is expected to eject a shell with velocities on the order of hundreds of km s^{-1} (Kovetz & Prialnik 1994; Shankar, Livio, & Truran 1991). However, the long-slit spectrum of CS93 shows that the velocities in the inner regions of the nebula (ring 1) are of the order of 10 km s^{-1}. Second, the likely candidate for the star that donates material to the hot star is a red giant, but the observed 2 μm flux density of 0.033 Jy (see § 3.3) is much lower than that expected for a red giant. For example, a $L = 3000\ L_{\odot}$ red giant with $T_{eff} = 3000$ K produces a flux density of roughly 5.5 Jy at 2.4 kpc. Finally, this model also does not explain the offset of the central star with respect to the large hourglass structure.

The third mechanism invokes the binarity of the central star (the companion to which is not seen and so must be less luminous). This admits the two cases of a close binary with a separation less than about 100 AU and a wide binary with a larger separation. Soker, Rappaport, & Harpaz (1998) have presented an analytical, highly idealized model of a

[12] Because [O III] is much more centrally confined than [N II], the [O III] expansion velocity, 10 km s^{-1}, more accurately represents the expansion of the waist region.

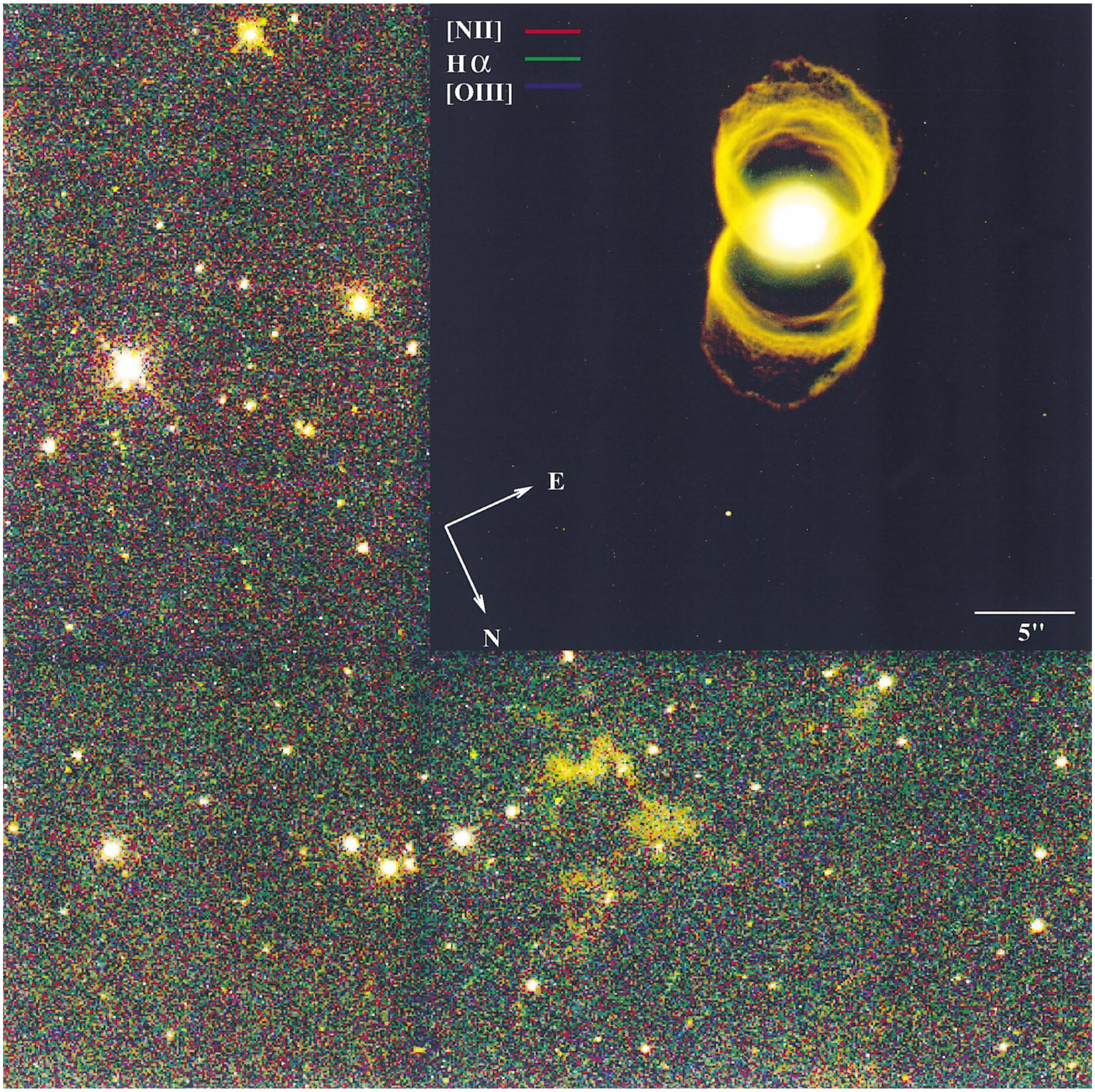

FIG. 5.—Composite color mosaic of [N II] (*red*), Hα (*green*), and [O III] (*blue*) images from all four cameras in WFPC2. The intensities in the main nebula on the PC chip have been decreased by a factor 10 compared with the other 3 WF chips. The faint yellow nebulosities seen north of the main nebula represent low-excitation gas that was ejected from the central star at significantly higher speeds than the expansion velocity of the main nebula.

close binary. The basic idea is that the net outflow speed of the ejected mass, averaged over many orbital cycles, might be different in different directions, and this will lead to an offset in the star's position from the center of symmetry of the resulting AGB CSE. This model may account for the offset of the central star from the center of ring 1, but it does not explain the offset of the star from the center of the extended hourglass structure. Nonetheless, we believe that it provides a plausible mechanism for producing an offset between the location of the central star and the center of symmetry of its ejecta, and it deserves to be explored in greater detail.

For wide binaries, the orbital period may be comparable to or longer than the ejection timescale of the slow wind. Soker (1994) concludes that this will not only result in a displacement of the star but may also produce large deviations from axisymmetry in the AGB CSE. Since MyCn 18 appears to have a well-defined axis of symmetry, a wide-binary scenario appears unlikely.

Our F547M image enables us to constrain the luminosity of any well-separated companion to the central star. Although this constraint is not useful for the close-binary model (Soker et al. 1998), it may be of value for new theoretical models. We find that the 3 σ lower limit on m_V for companions with separation of 500–1000 AU is 20.3–23.8 mag. The corresponding luminosity upper limits are roughly 0.1–0.004 $L_{\odot}$, if the companion is a cool star with $T_{\rm eff} \sim 3500$ K, and roughly 25–1 $L_{\odot}$ if it is a hot white dwarf with $T_{\rm eff} \sim 10^5$ K.

A binary star scenario is attractive for other reasons. Directly or indirectly, binarity can produce asymmetries through the formation of a dense equatorial accretion/

excretion disk (Morris 1987), high-velocity collimated outflows (Soker & Livio 1994; ST98), or an equatorially flattened common envelope (Livio 1993). In these contexts, ring 1 may find a natural explanation as the dense equatorial waist of an hourglass-shaped PN produced via the GISW scenario. However, the origins of ring 2 and the inner hourglass still remain a puzzle. It is noteworthy that inner and outer hourglass structures have been shown to exist in two other evolved objects whose central stars are symbiotic binaries—through direct imaging in the case of He 2-104 (CS93; ST98) and through analysis of long-slit spectroscopic observations in R Aqr (Solf & Ulrich 1985). R Aqr also shows a jetlike outflow whose axis has changed over time (Hollis, Pedelty, & Kafatos 1997), supporting ST98's hypothesis that such outflows play an important role in the shaping both of PNs in general and MyCn 18 in particular (§ 4.1).

5. CONCLUSIONS

We have obtained emission-line and continuum images of MyCn 18 with the WFPC2 on *HST*. These images show an hourglass-shaped structure. A series of arcs appear to be etched on the walls of the larger, outer hourglass near its rims, giving it its name. Faint, distant, low-excitation blobs are found near the long axis of the nebula. These are probably part of the high-velocity bipolar outflow that has been observed previously in MyCn 18.

In the complex central region of the nebula, we find a smaller, inner hourglass and two rings. Ring 1 is a bright elliptical ring defining the outer hourglass waist. Ring 2 is a smaller, higher excitation ring. The inner and outer hourglasses, as well as ring 1 and ring 2, have different centers, and none are centered on the central star.

Although the GISW model for planetary nebula formation can qualitatively explain the shape and kinematics of the outer hourglass, the complex inner nebular structure and the offsets of the central star from the center of the nebula components remain a mystery. We believe that it is likely that a successful explanation of these will involve a binary central star.

This work was supported by NASA grant NAS 7-1260 to the WFPC2 Investigation Definition Team. We are grateful to Will Henney, Mark Morris, and Michael Richer for useful suggestions.

REFERENCES

Acker, A., Jasniewicz, G., Köppen, J., & Stenholm, B. 1989, A&AS, 80, 201
Acker, A., Ochsenbein, F., Stenholm, B., Tylenda, R., Marcout, J., & Schohn, S. 1992, The Strasbourg-ESO Catalogue of Galactic Planetary Nebulae (Garching: ESO)
Balick, B. 1987, AJ, 94, 671
Balick, B., Preston, H. L., & Icke, V. 1987, AJ, 94, 1641
Blondin, J., & Lundqvist, P. 1993, ApJ, 405, 337
Borkowski, K. J., Blondin, J. M., & Harrington, J. P. 1997, ApJ, 482, L97
Brown, R. L., & Mathews, W. G. 1970, ApJ, 160, 939
Bryce, M., López, J. A., Holloway, A. J., & Meaburn, J. 1997, ApJ, 487, L161
Burrows, C., et al. 1995, ApJ, 452, 680
Corradi, R. L. M., & Schwarz, H. E. 1993, A&A, 268, 714
Dayal, A., et al. 1999, in preparation
Dwarkadas, V. V., & Balick, B. 1998, ApJ, 497, 267
Garcia-Segura, G., Langer, N., Rozyczka, M., & Franco, J. 1998, ApJ, submitted
Garcia-Segura, G., & Mac Low, M.-M. 1994, in Circumstellar Media in the Late Stages of Stellar Evolution, ed. R. E. S. Clegg, & I. R. Stevens, & W. P. S. Meikle (Cambridge: Cambridge Univ. Press), 85
Gleizes, F., Acker, A., & Stenholm, B. 1989, A&A, 222, 2
Harrington, J. P., Lame, N. J., White, S. M., & Borkowski, K. J. 1997, AJ, 113, 2147
Herman, J., Burger, J. H., & Penninx, W. H. 1986, A&A, 167, 247
Hollis, J. M., Pedelty, J. A., & Kafatos, M. 1997, ApJ, 490, 302
Jura, M. 1986, ApJ, 303, 327
Kovetz, A., & Prialnik, D. 1994, ApJ, 424, 319
Kwok, S., Purton, C. R., & Fitzgerald, P. M. 1978, ApJ, 219, L125
Livio, M. 1993, in IAU Symp. 155, Planetary Nebulae, ed. R. Weinberger & A. Acker (Dordrecht: Kluwer), 279
Mayall, M. W., & Cannon, A. J. 1940, Harvard Obs. Bull., No. 913, 7
Mellema, G. 1993, Ph.D. thesis, Sterrewacht Lieden
Morris, M. 1987, PASP, 99, 1115
Osterbrock, D. E. 1989, Astrophysics of Gaseous Nebulae and Active Galactic Nuclei (Mill Valley, CA: Univ. Sci.)
Sahai, R., Hines, D. C., Kastner, J. H., Weintraub, D. A., Trauger, J. T., Rieke, M. J., Thompson, R. I., & Schneider, G. 1998a, ApJ, 492, L163
Sahai, R., & Trauger, J. T. 1998, AJ, 116, 1357
Sahai, R., et al. 1998b, ApJ, 493, 301
Sahai, R., Wootten, A., Schwarz, H. E., & Clegg, R. E. S. 1991, A&A, 251, 560
Schwarz, H. E., Corradi, R. J. M., & Melnick, J. 1992, A&AS, 96, 23
Shankar, A., Livio, M., & Truran, J. W. 1991, ApJ, 374, 623
Soker, N. 1994, MNRAS, 270, 774
Soker, N., & Livio, M. 1994, ApJ, 421, 219
Soker, N., Rappaport, S., & Harpaz, A. 1998, ApJ, 496, 842
Solf, J., & Ulrich, H. 1985, A&A, 148, 274
te Lintel Hekkert, P., Chapman, J. M., & Zijlstra, A. A. 1992, ApJ, 390, L23
Trauger, J. T., et al. 1994, ApJ, 435, L3
Tylenda, R., Acker, A., Stenholm, B., Gleizes, F., & Raytchev, B. 1991, A&AS, 89, 77
Vishniac, E. T. 1994, ApJ, 428, 186
Young, K., Serabyn, G., Phillips, T. G., Knapp, G. R., Güsten, R., & Schulz, A. 1992, ApJ, 385, 265
Zhang, C. Y., Harvey, P. M., Smith, B. J., Colomé, C., & DiFrancesco, J. 1994, ApJ, 425, 687